

# Simulating the electrostatic patch force in sphere-plate and plate-plate geometries

Matthijs H. J. de Jong<sup>1</sup> and Laure Mercier de Lépinay<sup>1,\*</sup>

<sup>1</sup>*Department of Applied Physics, Aalto University, FI-00076 Aalto, Finland*

(Dated: August 30, 2024)

Potential patches are responsible for a force between closely-spaced objects that forms a parasitic contribution to sensitive force measurements. Existing analytical models cannot account for the patch force in the 3D geometries of real experiments. Here, we present a finite-element method model to evaluate the impact of patches in arbitrary geometries. First, we test our model against the plate-plate and sphere-plate geometries, for which the exact solutions are known. Then, we apply it to the analytically unwieldy case of plate-concave plate that is relevant for Casimir force measurements. This work provides a reliable estimation of the parasitic contribution from random potential patches.

The surface of real-world materials features spatial fluctuations of the effective electrostatic potential known as potential patches [1]. These patches can arise from local variations in the work function due to grain orientation [2], adsorbates [3], or defects [4]. These potential patches exert a force even after the mean potential difference between surfaces is removed, and thus they produce a parasitic signal in precision force measurements. Potential patches affect gravitational wave detectors [5–8], tests of general relativity [9], inverse-square law experiments [10–13], exclusions of non-Newtonian forces [14, 15], Casimir force experiments [16], AFMs [17], and particles suspended in traps [18, 19].

The patch contribution has been estimated to contribute < 1% of the force signal in extremely careful measurements of the Casimir force [20–25]. This magnitude has to be placed in the context of a discrepancy between the measured and predicted Casimir force between real (lossy) metal objects [26]. The parasitic patch force can be statistically estimated and was found to be significant on the level of the discrepancy, but fell short of bridging the difference between the theory and observations. Recent proposals on the measurement of the difference in Casimir force between superconducting and normal metals [27, 28], which can be expected to shed light on the discrepancy, face tighter constraints on the parasitic patch contribution. The difference in Casimir force between superconducting and normal plates is expected to be several orders of magnitude smaller than the Casimir force itself [28]. While potential patches can be measured using Kelvin Probe Force Microscopy (KPFM) [24] and reduced by surface treatments [25, 29], these methods are often not available in situ [30]. In this context, new undertakings in proximity force measurements should systematically be paired with a detailed investigation of the patch contribution in the experimental geometry used.

Thus, a large body of work has focused on modeling the effect of potential patches. The seminal paper on estimating the force from potential patches, [16], provides an analytic model based on spatial voltage correlations in and between two flat planes [23, 31]. This treatment has been extended to sphere-plate geometries using the proximity force approximation (PFA) [32] and transposed to a bi-spherical coordi-

nate system to describe the same geometry without using the PFA [33]. However, despite its relevance in Casimir force experiments, this last model has hardly been applied to experimental situations because of its complexity. Furthermore, innovative experiments studying the impact of Casimir forces in the context of cavity optomechanics involve more complicated geometries [27] are not suitable for analytic treatments. As a result, there is a growing interest for a practical and applicable simulation method to predict the patch force in a given geometry. Recently, a finite-element model was created that generates a random patch realization in a plate-plate geometry [34], but there remains a significant challenge in extending this method to arbitrary 3D geometries, which are more relevant in practice.

In this Letter, our goal is to describe a method to accurately estimate the parasitic contribution of patches in any experimental geometry. With input of patch properties from KPFM measurements on flat pieces of material, we can synthesize patch textures and apply them to the 3D surface of interest. To reach this goal, we create a finite-element model of randomly distributed potential patches that can handle non-planar (sphere-plate) and more complex geometries, and make it publicly available (see [Data availability](#)). We then study the scaling of the patch force with distance for different sphere radii and patch sizes, and make general recommendations to reduce the parasitic contribution of patches.

*Sphere-plate electrostatics* — We first consider the simple electrostatic force between a sphere and a plate when they are brought to (uniform) different potentials. The electrostatic energy density  $U$  is calculated in COMSOL and plotted in Figs. 1A,B. We take a small sphere (Fig. 1A), of radius  $R = 100$  nm separated by  $d = 100$  nm from the plate (point of closest approach), and a large sphere with radius  $R = 100$   $\mu$ m (Fig. 1A) at the same  $d$  and for the same  $V = 200$  mV potential difference. While the energy is delocalized around the small sphere in Fig. 1A, it is confined around the point of closest approach for the large sphere in Fig. 1B. This justifies truncating the geometry to a given radius  $R_{\text{sim}}$  for larger spheres, as it is necessary to manage computing resources in subsequent simulations of patch textures. Additionally, in some experiments, the truncated sphere is an accurate representation of the geometry [35, 36].

The electrostatic force  $F = \partial U / \partial d$  is calculated by repeating the simulations for various distances, and shown in

\* [laure.mercierdelepinay@aalto.fi](mailto:laure.mercierdelepinay@aalto.fi)

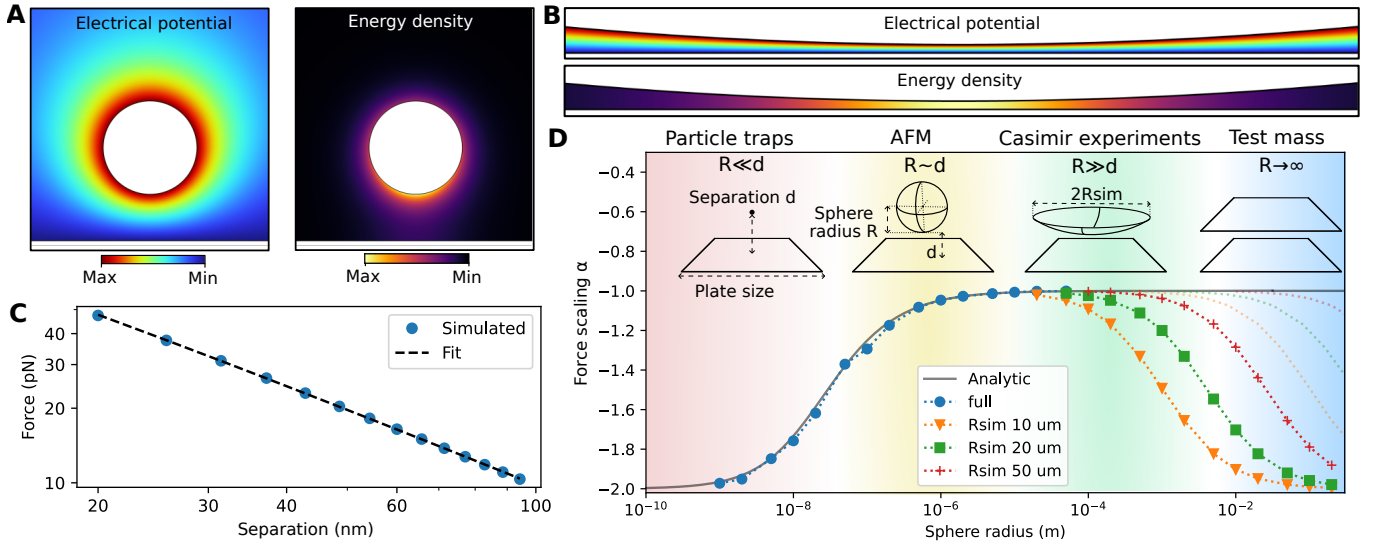


FIG. 1. **A,B**: Simulated electric potential and energy density in the small-sphere and large-sphere limits. The sphere is separated from the plate below by 100 nm at the closest approach in both limits. While the energy density is distributed all around the small sphere, it is focused at the closest approach in the large sphere. All plots are 2D plane cuts through the center of the 3D-simulated sphere and plate. **C**: To extract the force-distance scaling, we run the finite-element model for different spacing  $d$  between sphere and plate (blue circles), and fit a straight line in log-log scale (black dotted line). **D**: Distance-scaling of the electrostatic force between a sphere and plate. The exact solution (solid black line) yields  $F \propto d^{-2}$  for  $R \ll d$ , and  $F \propto d^{-1}$  for  $R \gg d$ . Our finite-element model containing the whole sphere (blue circles) reproduces the exact solution, but truncating the model to limited size (orange triangles, green squares, and red crosses) deviates towards the parallel-plate solution  $F \propto d^{-2}$ . The transparent, dotted curves are extrapolated to factor 10 larger simulation sizes than the opaque curves of the same color. Insets: schematic representation of the sphere-plate simulations.

Fig. 1C. It scales like a power law,  $F \propto d^\alpha$ , and the exponent  $\alpha$  is extracted by a fit. The force is shown to scale as  $\alpha = -2$  for  $R \ll d$  and as  $\alpha = -1$  for  $R \gg d$  in Fig. 1D, as can be derived from the exact solution [32, 37]

$$F = -2\pi\epsilon_0 V^2 \sum_{n=1}^{\infty} \frac{1}{\sinh(n\beta[\coth(\beta) - n\coth(\beta)])}. \quad (1)$$

Here  $\beta = \text{arccosh}\left(1 + \frac{d}{R}\right)$ ,  $V$  is the potential difference between sphere and plate and  $\epsilon_0$  the vacuum permittivity. In the truncated finite-element model,  $\alpha$  tends to  $-2$  in the limit of large sphere radius, matching the expected exponent for the force between two plates, but in contradiction with the analytical formula of Eq. (1). The radius at which this happens depends on the truncation radius  $R_{\text{sim}}$ , which indicates that this behavior is an artefact of the truncation. This simple electrostatic study allows us to define the domain of validity of the model that we shall use for simulations of patches.

*Patch potential model* — We now turn to modelling the force arising from electrostatic patches. The electrostatic force  $F$  due to potential patches can be computed for two infinite parallel plates, [16]

$$F = -\frac{\epsilon_0}{2(2\pi)^2} \iint \frac{k^2}{\sinh^2(kd)} (C_{11} + C_{22} - 2C_{12} \cosh(kd)) \sin(\theta) d\theta dk, \quad (2)$$

as long as the plate's separation is much smaller than the plate's lateral dimensions. The 2D reciprocal coordinates  $k_x$

and  $k_y$  are used, and we transform to polar coordinates with angle  $\theta$  and  $k^2 = k_x^2 + k_y^2$  before integrating.  $C_{11}(\theta, k)$ ,  $C_{22}(\theta, k)$ , and  $C_{12}(\theta, k)$  are the spatial spectral densities of the potential distributions  $V_1$  and  $V_2$  on plates 1 and 2 respectively. They are defined by  $C_{ij} = \langle V_i(\theta, k) V_j(\theta + \pi, k) \rangle$ .

For a sphere-plate system, the full expression for the force without approximations is rather complicated [33], but a simpler case can be worked out by applying the PFA [16]. This approximation supposes a tessellation of the patches on the sphere into ring-like elements parallel to the plate, valid when  $kd \ll 1$  and  $R \gg d$ . The force can be written as [16]

$$F = -\frac{\pi\epsilon_0 R}{(2\pi)^2} \iint \frac{k((C_{11} + C_{22})e^{-kd} - 2C_{12})}{\sinh(kd)} \sin(\theta) d\theta dk. \quad (3)$$

While there have been discussions about the precise statistical properties of  $C_{11}$ ,  $C_{22}$ , and  $C_{12}$  [16, 23, 34], it is generally accepted that patches are uncorrelated at large distances, i.e., for  $\lim_{k \rightarrow \infty} C_{ii} = 0$  and  $C_{12} = C_{21} = 0$  everywhere (uncorrelated plates). Other than these considerations, the statistical properties of patches in a given material can be extracted from KPFM measurements [24]. Here, we focus on the simulation method and use a standard statistical model for the patches. To estimate the expected parasitic patch force, we average over random realizations of patches, similar to Ref. [34]. The crux of this approach is that it is difficult to map a randomized patch texture on an arbitrarily curved experimental geometry. The surface geometry of an experimental apparatus may be difficult to parameterize. This hinders the generation of textures of random patches that exactly follow the (curved) surface. For

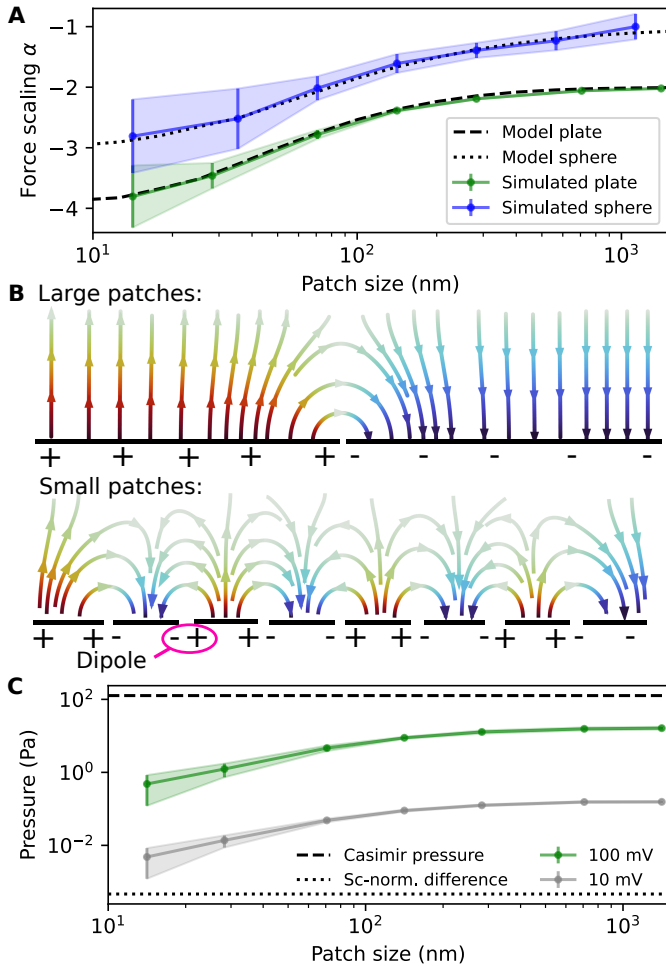


FIG. 2. **A**: Distance-scaling of the patch force between two plates (green shaded area) and sphere-plate (blue shaded area). The solid line is the average scaling from 10 sets of  $\geq 200$  randomized patches, while the shaded area spans the standard deviation of the scaling (67% confidence interval). Dashed and dotted lines are the model of [16] evaluated numerically. **B**: Schematic of the electrical field in the case of small patches (left) and large patches (right). **C**: Patch pressure for 100 mV standard deviation patches for plates 60 nm apart. The patch force decreases with smaller patch size once  $\ell \not\gg d$ . It is much smaller than the Casimir pressure between the plates, but much larger than the proposed effect of the superconducting transition on the Casimir pressure.

sufficiently flat geometries, we can generate a plane (2D) distribution of patches and extrude it to a target surface [34]; this will not distort the spatial spectral densities  $C_{11}$ ,  $C_{22}$ , and  $C_{12}$ . However, projecting a 2D patch texture on a geometry that is curved in 3D deforms the patches and changes the spatial spectral densities.

Our approach is as follows: We first generate a set of random coordinates in a 3D volume containing the surfaces of interest to be the patch centers. Then, we compute a 3D Voronoi diagram either with Scipy [38] or MATLAB [39]. We then compute the intersections of the Voronoi cells with an arbitrarily curved experimental geometry in COMSOL [40]. The

intersections are used to subdivide the surface of the experimental geometry, which results in patches that have the same size characteristics as the Voronoi diagram regardless of the curvature of the surface. Finally, we assign electrostatic potential with a random, normally distributed, value to each of the patches. In the example of a small sphere close to a plate, our toolbox generates patches at the equator that have the same average size as those at the poles, where the approach to the plates is the closest (see also Supplementary Secs. IA and IB). We have made our toolbox and methods publicly available (see Data availability), and now use it to study the patch force behavior in some standard geometries.

*Scaling exponent* — We plot the patch force scaling exponent  $F \propto d^\alpha$  as a function of the average patch size  $\ell = \sqrt{A/n_{\text{patch}}}$  where  $A$  is the area of the simulated surface and  $n_{\text{patch}}$  the number of patches. As shown in Fig. 2B, for large patches,  $\ell \gg d$ , the force scales similarly to the patchless case,  $\alpha = -2$  (plate-plate) or  $\alpha = -1$  (sphere-plate). On the other hand, for small patches,  $\ell \ll d$ , the force scales as  $\alpha = -4$  (plate-plate) or  $\alpha = -3$  (sphere-plate), similar to the Casimir force between perfect conductors. Intuitively, for large patches, the majority of the electrostatic energy exists between patches on opposite plates, and there is very little interaction between patches on the same plate. Hence, it behaves similarly to the plain electrostatic case presented in the first part of this Letter. For small patches, the interaction between patches on the same plate is much stronger than the interaction between patches on different plates. The interfaces between patches can be seen as a dipole oriented in the plane of the plate, the force between two distributions of dipoles is known to scale with  $\alpha = -4$ .

Our finite element simulations clearly match the theory models across all patch sizes in Fig. 2A, for both the sphere-plate and plate-plate geometries. The variance in force-distance scaling increases as the patches shrink: Patches interact with a wider area of the opposite object if the objects are separated by more than the patch size. This is caused by the finite number of patches considered in our simulations (typically  $> 200$  patches per side), but also in the theory evaluation (100,000 patches). Especially the sphere-plate geometry is susceptible to this spread in scaling, since some parts of the sphere are naturally closer to the other object, and thus the exact realization of the patches matters.

*Patch force magnitude* — We plot the total pressure as a result of the potential patches in Fig. 2C. For patches normally distributed in potential with a standard deviation of 100 mV, two plates separated by 60 nm experience  $16 \pm 1.4$  Pa pressure in the large-patch limit (green line). The pressure decreases as the patch size decreases, but the relative variance (pressure variance divided by pressure) increases due to the wider interaction area, similar to the scaling. Compensating the mean potential with an offset (to the electrostatic zero) yields a negligible reduction in the force. To reduce the parasitic contribution of potential patches in force-sensing experiments, one should use materials with small patch sizes. Evaporated thin films with small crystal grains are likely to have smaller patches than bulk materials, so depositing a thin metal film on the relevant experimental parts should prove beneficial in reducing

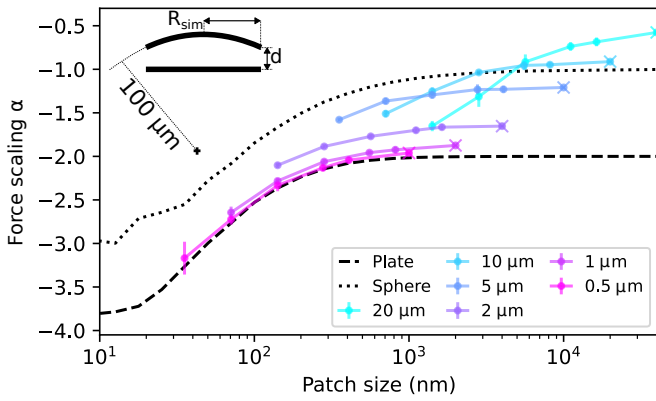


FIG. 3. Force-distance scaling for a geometry where the top plate bulges upwards as in superconducting drum resonators (inset schematic). For small drums, the scaling follows the model of two flat plates. For larger drums, the scaling flattens out and tends to becoming independent of distance ( $\alpha = 0$ ) as it would be for a ring. Numerical models (dashed and dotted lines) are from Ref. [16]. Legend entries are the simulation size  $R_{\text{sim}}$ , the crosses indicate the scaling in the case without patches.

the patch contribution.

A normal distribution with a 10 mV standard deviation is more in line with the variation of work function across crystallographic orientations within a single material. This distribution yields a smaller pressure by two orders of magnitude (Fig. 2C grey line), reflecting the  $V^2$  scaling of the electrostatic force. In line with literature [20, 22–25], the patch pressure is much smaller than the Casimir pressure in this geometry (dashed line, 126.87 Pa). However, the patch contribution will dominate the recently proposed experiments to observe the Casimir pressure difference between superconductors and normal-state conductors (dotted line, 0.46 mPa [28]) if the patch texture changes between the two states. This result emphasizes the importance of accurately evaluating the patch contribution in the experimental geometry.

*Bulging drum geometry* — We have so far discussed geometries where analytic solutions are available. The strength of our finite-element formulation is that we are not confined to these geometries, so we study a bulging-plate model for which we know of no analytic solution. This geometry is motivated because superconducting optomechanical drum resonators [41, 42], which can be favorably adapted to study the Casimir force, are generally observed to bulge or sag. We take a 100  $\mu\text{m}$  radius-of-curvature for the bulging, which yields a 500 nm height difference between the center and rim of a 10  $\mu\text{m}$  drum. In the context of these drums, this represents an extreme bulging case. We plot the force-distance scaling for various drum radii in Fig. 3. The plate separations we simulate are between 20 – 120 nm.

It is clear from Fig. 3 that the force-distance scaling depends on the drum’s radius. For the largest drums the force becomes almost independent of the distance ( $\alpha = 0$ ). This can be understood by realizing that all the electrostatic energy is focused between the outer rim of the drum and the plate, as

the center of the drum is far away from the plate. The electric field close to the surface of a disk is independent of distance to the disk. However, this behavior requires the disk to be uniformly charged (or at the same potential), and it is thus very sensitive to patches. We interpret this property to be the reason why the force-distance scaling grows quickly with patch size. For a fixed radius of curvature, smaller drums are relatively flatter than larger drums, so the force scales as in the plate-plate geometry ( $\alpha = -2$ ).

*Conclusion* — We have modeled the parasitic contribution from electrostatic patches in a complex 3D geometry for the first time. Our results match analytic or approximate results for the geometries where they are available, and we have found an intuitive explanation for the force-distance scaling in the limit of large and small patches. We have also simulated the force-distance scaling of the patch contribution in bulging drum resonators, for which no analytic solution is available. Our models can be adapted to any 3D geometry, and can thus be used to accurately estimate the patch contribution in sensitive force experiments. To minimize the patch contribution, one should choose materials with small patch sizes (patch size  $\ell \ll d$ , the distance between plates), and materials with a narrow potential distribution of the patches. These properties will also reduce the uncertainty in the patch force. Thin-film materials appear advantageous over bulk materials, as the typical crystal size is related to the layer thickness, and ideally the work function should be similar in all crystal orientations. Our method allows us to compute the parasitic contribution from potential patches in any experimental geometry, which will improve the fidelity of Casimir force experiments and other small-force sensing experiments. We hope that this Letter and our model can be of use to the community wherein everyone is invited to measure the patches of their specific material(s) and run them through our simulation.

#### Data availability

All data, simulations, measurement and analysis scripts in this work are available at <https://doi.org/10.5281/zenodo.13255585>.

#### Acknowledgments

M.J. and L.M. acknowledge the Aalto Scientific Computing team for their support. L.M. acknowledges funding from the Strategic Research Council at the Academy of Finland (Grant No. 338565).

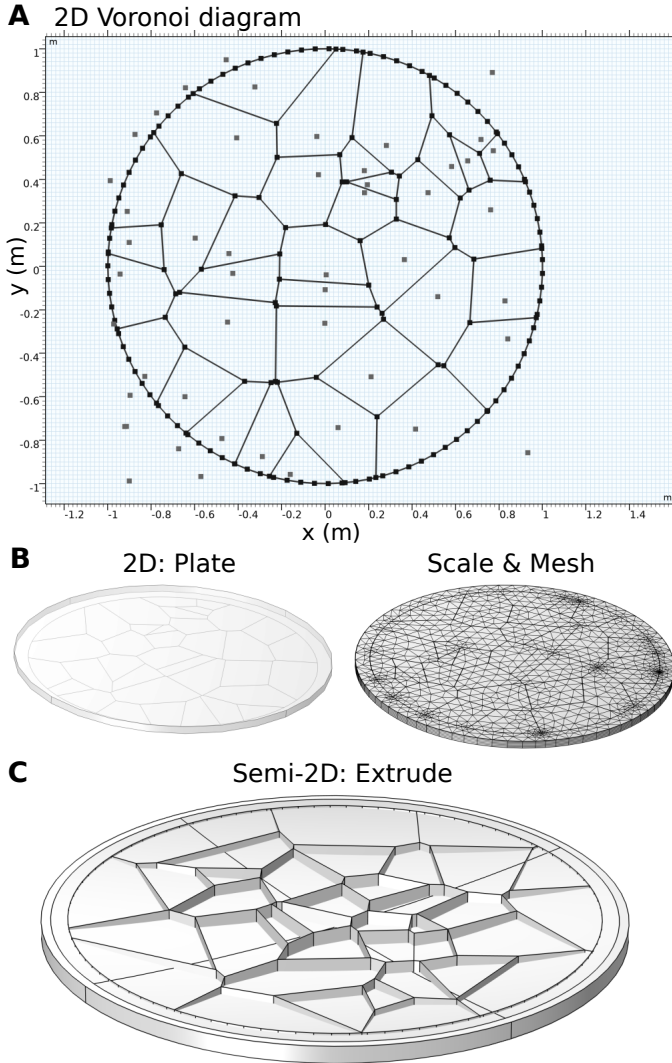


FIG. S1. **A** We generate a set of random points in a square with side lengths 2 m centered around the origin. We then compute a Voronoi diagram within a circular radius. **B** For a truly 2D geometry, the Voronoi diagram is created on a work plane, we scale it to the desired size and generate a finite element method mesh. **C** For a semi-2D geometry, we extrude the Voronoi diagram until it intersects the curved geometry part completely. The scale and mesh steps proceed in the same fashion as the truly 2D geometry.

## I. SUPPLEMENTARY INFORMATION

### A. Geometry sequence of patches

Generating the simulation geometry with randomized patches is somewhat challenging. The complete MATLAB script responsible for generating the geometry and running the simulations, as well as a selection of the solved models, can be found in the publicly available dataset (see [Data availability](#)).

For a 2D geometry, we follow the method of Ke et al. [34]. We generate a set of random points in plane and compute its Voronoi diagram (Fig. S1A). We choose for a circular geom-

etry, as that avoids sharp corners and matches the geometry of our future experiments. We approximate the circle by a 100-point polygon, and use the code of Ref. [39] to generate the Voronoi diagram. The set of random points and the Voronoi diagram are created in MATLAB, and they are then exported to COMSOL in a work plane (2D). For the plate-plate simulations, we simply take the work plane geometry as the boundary of a cylinder, Fig. S1B. We repeat this process for the second plate and join the two plates into a single model. We assign potentials to each of the patches based on a normal distribution (MATLAB function `normrnd`). Since the geometry tends to be rather flat (large aspect ratio), we generate a structured mesh to ensure sufficient resolution in the out-of-plane direction (Fig. S1B).

If the geometry is not perfectly flat, we can make an approximation: We generate the patches in 2D using the above method, but then extrude and use Boolean operations so project the patches onto a semi-2D surface (Fig. S1C). In the case of a sphere with a radius of curvature much larger than the separation with the plate, the error is small and focused in the patch size of the patches at the outer edge of the simulation. This is analogous to taking the proximity force approximation [32].

The power of our finite-element model of patches is that we can handle patches in 3D, to match the actual geometry of the experiments. Conceptually, the method of generating the geometry is the same in 3D as it is in 2D. The same code [39] can generate both 3D and 2D Voronoi diagrams, but importing the geometry into COMSOL is more involved in the 3D case. In Fig. S2, we have generated 400 patches on a hemisphere of diameter  $1 \mu\text{m}$ , and 1600 patches on the plate below ( $2 \mu\text{m}$  diameter). For the sphere, we chose to generate the random points such that they are all on the surface of the sphere. This way, our simulation scales more favorably with the number of points.

Our code uses many of the Boolean operations `Extrude`, `Partition domains`, and `Union` that COMSOL offers, and we have made our scripts available in the public dataset (see [Data availability](#)) to facilitate replication and use of our method in other experimental geometries. Modeling the patches in 3D properly takes into account the surface curvature and avoids approximations such as the proximity force approximation [32]. However, this comes at a cost of increased computation time. Many of the simplifications one would normally make to generate a finite-element mesh cannot be made due to the randomness of the geometry. Nonetheless, we can solve the electrostatic problem of the sphere-plate with patches, as shown by the potential plotted in Fig. S2B.

### B. Numerical model of patch force in Python

The patch model of Ref. [16] treats patches in a statistical fashion. For any realization of (random) patches, the spatial correlations are computed;  $C_{11}$  and  $C_{22}$  for patches on the same plate and  $C_{12}$  between the patches on different plates. The electrostatic energy of the patches is then computed based on these correlations and the geometry of the plates. Dif-

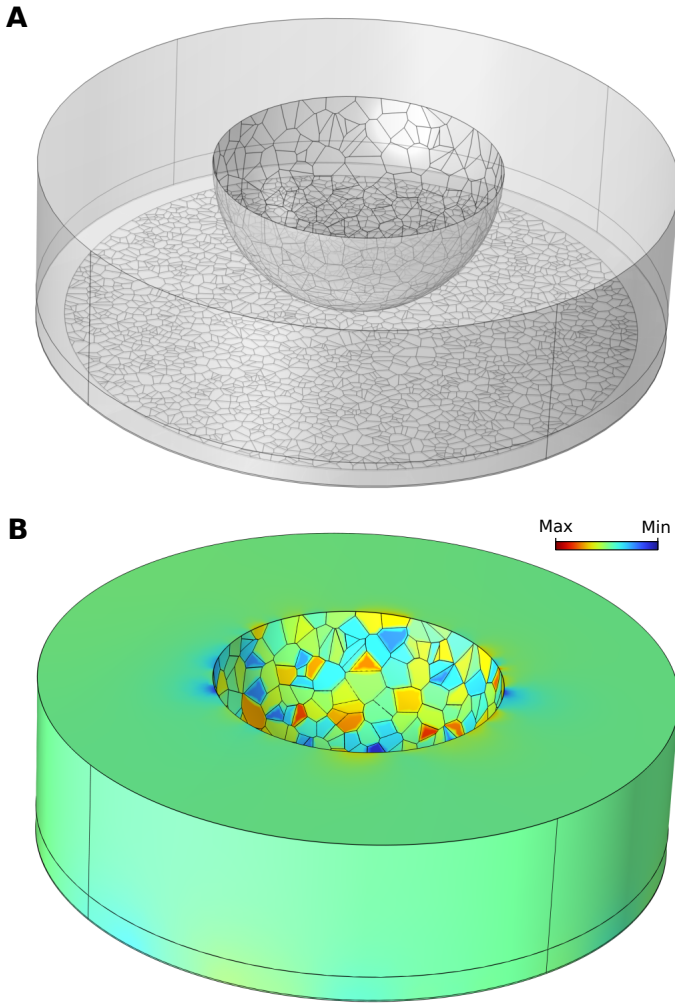


FIG. S2. **A** For 3D geometries, we generate random points in a 3D cube with side lengths 2 m around the origin, and compute the Voronoi diagram as in the 2D case. The translation of Voronoi diagram to geometry in COMSOL is more computationally intensive than in the 2D case. For some 3D geometries, we generate the random points to lie only on the surface of the final object (hemisphere, in this case). **B** We generate a 3D mesh, randomize the potentials assigned to each patch and solve the electrostatic problem. Since the patch interaction is between plate and (hemi-)sphere, we do not include the internal domain of the (hemi-)sphere.

ferent statistical descriptions of patches have been proposed, e.g., the sharp-cutoff model that assumes that all patches fall

between a minimum and maximum size [16], and the quasi-local model that sums over all (circular) patches that contain any two points on the plate [23]. We follow the model of Ref. [34] by generating the patches using Voronoi diagrams of randomly distributed points, which is a well-known way of modeling polycrystalline solids.

We use `scipy` [38] to generate the Voronoi diagram for a number of randomly distributed points. We then assign a random potential value to each region (grain) by filling the area with a random greyscale color using `matplotlib`. We save the resulting image and subsequently use the pixelation as a spa-

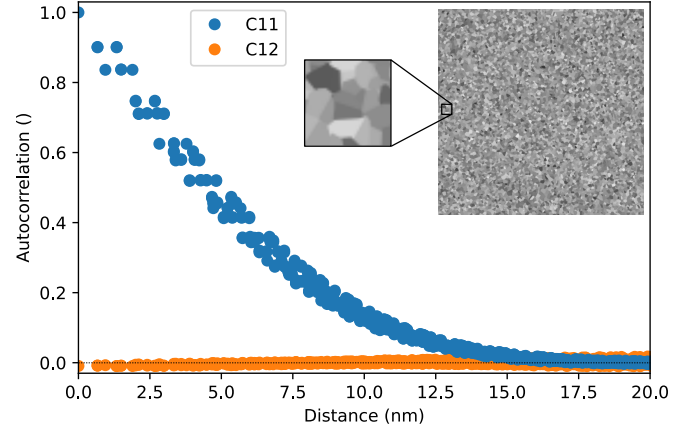


FIG. S3. Autocorrelation function of the Voronoi diagram used to model patches, with the patches and their (greyscale) potential shown as an inset. This model has 10,000 patches in a  $1 \times 1 \mu\text{m}^2$  area, for an average patch size of 10 nm. The zoom-in covers a  $50 \times 50 \text{ nm}^2$  area and shows the discretization (pixelation) used for the numerical analysis.

tial discretization of the domains. We subtract the average greyscale value of all the pixels to obtain a Gaussian distribution centered around zero. The correlations  $C_{11}$ ,  $C_{22}$  and  $C_{12}$  can be directly computed from the image matrices using `scipy`. An example Voronoi diagram is shown in Fig. S3 (inset), with the zoom-in showing the pixelation. The autocorrelation of potential (blue dots) shows a decreasing trend qualitatively similar to the quasi-local patch model of [23]. The cross-correlation between the shown Voronoi diagram and another patch realization generated using the same settings is shown with orange dots, and it is close to 0 everywhere.

[1] J. B. Camp, T. W. Darling, and R. E. Brown, *Journal of Applied Physics* **69**, 7126 (1991).  
 [2] S. Sadewasser, T. Glatzel, M. Rusu, A. Jäger-Waldau, and M. C. Lux-Steiner, *Applied Physics Letters* **80**, 2979 (2002).  
 [3] A. Yurtsever, D. Fernández-Torre, J. Onoda, M. Abe, S. Morita, Y. Sugimoto, and R. Pérez, *Nanoscale* **9**, 5812 (2017).  
 [4] T. Glatzel, S. Sadewasser, R. Shikler, Y. Rosenwaks, and M. C. Lux-Steiner, *Materials Science and Engineering B* **102**, 138

(2003).  
 [5] C. C. Speake, *Classical and Quantum Gravity* **13**, A291 (1996).  
 [6] N. A. Robertson, J. R. Blackwood, S. Buchman, R. L. Byer, J. Camp, D. Gill, J. Hanson, S. Williams, and P. Zhou, *Classical and Quantum Gravity* **26**, 2665 (2006).  
 [7] S. E. Pollack, S. Schlamminger, and J. H. Gundlach, *Physical Review Letters* **101**, 071101 (2008).  
 [8] S. Vitale, V. Ferroni, L. Sala, and W. J. Weber (2024), arxiv

preprint.

- [9] C. W. F. Everitt, D. B. DeBra, B. W. Parkinson, J. P. Turneaure, J. W. Conklin, M. I. Heifetz, G. M. Keiser, A. S. Silbergleit, T. Holmes, J. Kolodziejczak, M. Al-Meshari, J. C. Mester, B. Muhlfelder, V. G. Solomonik, K. Stahl, P. W. Worden Jr., W. Bencze, S. Buchman, B. Clarke, A. Al-Jadaan, H. Al-Jibreen, J. Li, J. A. Lipa, J. M. Lockhart, B. Al-Suwaidan, M. Taber, and S. Wang, *Physical Review Letters* **106**, 221101 (2011).
- [10] F. Antonucci, A. Cavalleri, R. Dolesi, M. Hueller, D. Nicolodi, H. B. Tu, S. Vitale, and W. J. Weber, *Physical Review Letters* **108**, 181101 (2012).
- [11] R. O. Behunin, D. A. R. Dalvit, R. S. Decca, and C. C. Speake, *Physical Review D* **89**, 051301 (2014).
- [12] W.-H. Tan, A.-B. Du, W.-C. Dong, S.-Q. Yang, C.-G. Shao, S.-G. Guan, Q.-L. Wang, B.-F. Zhan, P.-S. Luo, L.-C. Tu, and J. Luo, *Physical Review Letters* **124**, 051301 (2020).
- [13] W.-C. Dong, W.-H. Tan, Z.-J. An, H. Huang, L. Zhu, Y.-J. Tan, T.-Y. Long, C.-G. Shao, and S.-Q. Yang, *Physical Review Applied* **20**, 054046 (2023).
- [14] A. O. Sushkov, W. J. Kim, D. A. R. Dalvit, and S. K. Lamoreaux, *Physical Review Letters* **107**, 171101 (2011).
- [15] G. L. Klimchitskaya, U. Mohideen, and V. M. Mostepanenko, *Physical Review D* **86**, 065025 (2012).
- [16] C. C. Speake and C. Trenkel, *Physical Review Letters* **90**, 160403 (2003).
- [17] I. Dorofeyev, H. Fuchs, G. Wenning, and B. Gotsmann, *Physical Review Letters* **83**, 2402 (1999).
- [18] Q. A. Turchette, D. Kielpinski, B. E. King, D. Leibfried, D. M. Meekhof, C. J. Myatt, M. A. Rowe, C. A. Sackett, C. S. Wood, W. M. Itano, C. Monroe, and D. J. Wineland, *Physical Review A* **61**, 063418 (2000).
- [19] R. Dubessy, T. Coudreau, and L. Guidoni, *Physical Review A* **80**, 031402 (2009).
- [20] R. S. Decca, D. López, E. Fischbach, and D. E. Krause, *Physical Review Letters* **91**, 050402 (2003).
- [21] R. S. Decca, D. López, E. Fischbach, G. L. Klimchitskaya, D. E. Krause, and V. M. Mostepanenko, *Annals of Physics* **318**, 37 (2005).
- [22] R. S. Decca, D. López, E. Fischbach, G. L. Klimchitskaya, D. E. Krause, and V. M. Mostepanenko, *Physical Review D* **75**, 077101 (2007).
- [23] R. O. Behunin, F. Intravaia, D. A. R. Dalvit, P. A. Maia Neto, and S. Reynaud, *Physical Review A* **85**, 012504 (2012).
- [24] J. L. Garrett, D. Somers, and J. N. Munday, *Journal of Physics: Condensed Matter* **27**, 214012 (2015).
- [25] J. L. Garrett, J. Kim, and J. N. Munday, *Physical Review Research* **2**, 023355 (2020).
- [26] V. M. Mostepanenko, *Universe* **7**, 84 (2021).
- [27] R. A. Norte, M. Forsch, A. Wallucks, I. Marinković, and S. Gröblacher, *Physical Review Letters* **121**, 030405 (2018).
- [28] G. Bimonte, *Physical Review A* **99**, 052507 (2019).
- [29] J. Xu, G. L. Klimchitskaya, V. M. Mostepanenko, and U. Mohideen, *Physical Review A* **97**, 032501 (2018).
- [30] D. Garcia-Sanchez, K. Yan Fong, H. Bhaskaran, S. Lamoreaux, and H. X. Tang, *Physical Review Letters* **109**, 027202 (2012).
- [31] W. J. Kim, A. O. Sushkov, D. A. R. Dalvit, and S. K. Lamoreaux, *Physical Review A* **81**, 022505 (2010).
- [32] C. D. Fosco, F. C. Lombardo, and F. D. Mazzitelli, *Annals of Physics* **327**, 2050 (2012).
- [33] R. O. Behunin, Y. Zeng, D. A. R. Dalvit, and S. Reynaud, *Physical Review A* **86**, 052509 (2012).
- [34] J. Ke, W.-C. Dong, S.-H. Huang, Y.-J. Tan, W.-H. Tan, S.-Q. Yang, C.-G. Shao, and J. Luo, *Physical Review D* **107**, 065009 (2023).
- [35] W. J. Kim, A. O. Sushkov, D. A. R. Dalvit, and S. K. Lamoreaux, *Physical Review Letters* **103**, 060401 (2009).
- [36] R. S. Decca, E. Fischbach, G. L. Klimchitskaya, D. E. Krause, D. López, U. Mohideen, and V. M. Mostepanenko, *Physical Review A* **79**, 026101 (2009).
- [37] W. R. Smythe, *Static and dynamic electricity*, 3rd ed., edited by G. P. Harnwell, E. U. Condon, G. R. Harrison, E. Hutchinson, and K. K. Darrow, International Series in Pure and Applied Physics (McGraw-Hill Book Company Inc., 1989).
- [38] P. Virtanen, R. Gommers, T. E. Oliphant, M. Haberland, T. Reddy, D. Cournapeau, E. Burovski, P. Peterson, W. Weckesser, J. Bright, S. J. van der Walt, M. Brett, J. Wilson, K. Jarrod Millman, N. Mayorov, A. R. J. Nelson, E. Jones, R. Kern, E. Larson, C. J. Carey, I. Polat, Y. Feng, E. W. Moore, J. VanderPlas, D. Laxalde, J. Perktold, R. Cimrman, I. Henriksen, E. A. Quintero, C. R. Harris, A. M. Archibald, A. H. Ribeiro, F. Pedregosa, P. van Mulbregt, and Scipy 1.0 Contributors, *Nature Methods* **17**, 261 (2020).
- [39] H. Park, *Polytope bounded Voronoi diagram* (2020).
- [40] A. L. S. Oliveira, *Voronoi geometry using MATLAB and COMSOL* (2022).
- [41] J. D. Teufel, T. Donner, D. Li, J. W. Harlow, M. S. Allman, K. Cicak, A. J. Sirois, J. D. Whittaker, K. W. Lehnert, and R. W. Simmonds, *Nature* **475**, 359 (2011).
- [42] J. D. Teufel, D. Li, M. S. Allman, K. Cicak, A. J. Sirois, J. D. Whittaker, and R. W. Simmonds, *Nature* **471**, 204 (2011).